

Interfacial colloidal rod dynamics: Coefficients, simulations, and analysis

Yuguang Yang, and Michael A. Bevan

Citation: [The Journal of Chemical Physics](#) **147**, 054902 (2017); doi: 10.1063/1.4995949

View online: <https://doi.org/10.1063/1.4995949>

View Table of Contents: <http://aip.scitation.org/toc/jcp/147/5>

Published by the [American Institute of Physics](#)

Articles you may be interested in

[Effective colloidal interactions in rotating magnetic fields](#)

The Journal of Chemical Physics **147**, 074903 (2017); 10.1063/1.4986501

[Block copolymer templated self-assembly of disk-shaped molecules](#)

The Journal of Chemical Physics **147**, 054905 (2017); 10.1063/1.4993210

[Perspective: Dissipative particle dynamics](#)

The Journal of Chemical Physics **146**, 150901 (2017); 10.1063/1.4979514

[Radial distribution function of semiflexible oligomers with stretching flexibility](#)

The Journal of Chemical Physics **147**, 054901 (2017); 10.1063/1.4991689

[Brownian dynamics of a protein-polymer chain complex in a solid-state nanopore](#)

The Journal of Chemical Physics **147**, 054903 (2017); 10.1063/1.4995423

[Lattice animals in diffusion limited binary colloidal system](#)

The Journal of Chemical Physics **147**, 054904 (2017); 10.1063/1.4996739

PHYSICS TODAY

WHITEPAPERS

ADVANCED LIGHT CURE ADHESIVES

Take a closer look at what these environmentally friendly adhesive systems can do

READ NOW

PRESENTED BY
 **MASTERBOND**
ADHESIVES | SEALANTS | COATINGS

Interfacial colloidal rod dynamics: Coefficients, simulations, and analysis

Yuguang Yang and Michael A. Bevan^{a)}

Chemical and Biomolecular Engineering, Johns Hopkins University, Baltimore, Maryland 21218, USA

(Received 21 May 2017; accepted 13 July 2017; published online 1 August 2017)

Colloidal rod diffusion near a wall is modeled and simulated based on a constrained Stokesian dynamic model of chains-of-spheres. By modeling colloidal rods as chains-of-spheres, complete diffusion tensors are computed for colloidal rods in bulk media and near interfaces, including hydrodynamic interactions, translation-rotation coupling, and all diffusion modes in the particle and lab frames. Simulated trajectories based on the chain-of-spheres diffusion tensor are quantified in terms of typical experimental quantities such as mean squared positional and angular displacements as well as autocorrelation functions. Theoretical expressions are reported to predict measured average diffusivities as well as the crossover from short-time anisotropic translational diffusion along the rod's major axis to isotropic diffusion. Diffusion modes are quantified in terms of closed form empirical fits to model results to aid their use in interpretation and prediction of experiments involving colloidal rod diffusion in interfacial and confined systems. *Published by AIP Publishing.* [<http://dx.doi.org/10.1063/1.4995949>]

I. INTRODUCTION

Micro- and nano-sized colloidal rod-shaped particles are important in numerous dynamic processes involving, for example, biological macromolecules and micro-organisms¹ and novel building blocks in materials engineering.^{2,3} Rod-shaped colloidal particles experience Brownian translation and rotation that are important to dynamic processes including their transport and self-assembly. Colloidal rod collective dynamics are important to many phenomena such as phase transitions,⁴ packing,⁵ aggregation,⁶ and assembly.⁷ However, all aspects of single rod dynamics near surfaces are still not understood in terms of comprehensive models, which is important to problems involving transport in natural and biological porous media as well as rod assembly dynamics on substrates. Spherical colloidal particle motion near a wall has been accurately quantified in theory,⁸ simulations,^{9–11} and experiments,^{12–15} but for colloidal rods near a wall, the interplay of conservative (e.g., electrostatic) and non-conservative (i.e., hydrodynamic) forces in dynamics processes is significantly more complex.

Historically, some of the earliest relevant models for bulk rod diffusion were for cylinders¹⁶ and from slender-body theory for large aspect ratio particles.¹⁷ A method for treating rod shaped particles as collections of many small spheres more accurately accounted for end-effects for shorter aspect ratios, which have been corroborated in experiments.¹⁸ Other approaches such as boundary element¹⁹ and path integral²⁰ methods have produced increasingly accurate bulk rod transport properties. In addition to translational and rotational diffusion, rod particles have also been shown to exhibit a transition between short-time anisotropic translational diffusion

along the particle long-axis and long-time isotropic translation diffusion, which occurs after rotational diffusion that allows sampling of all translational modes. This effect is understood in two-dimensional (2D) systems²¹ but has not been studied for three-dimensional (3D) rod diffusion in bulk media or near walls.

For rods near a no-slip planar wall surface, the rod's translational and rotational diffusivities depend on aspect ratio, orientation, and separation relative to the wall. Models that capture some aspects of rod motion near surfaces include infinitely long cylinders adjacent to walls,²² slender-body theory for rods parallel or perpendicular to walls for separations comparable to the rod length,²³ chains-of-spheres for single aspect ratios vs. elevation and orientation using stochastic rotation dynamics,²⁴ multipole expansion of Green's function for axisymmetric particles near walls,²⁵ and finite element simulations of spheroid shaped particles near boundaries.²⁶ These previous studies have limitations either in terms of accurately capturing hydrodynamic interactions important to rod translation and rotation near surfaces or in terms of probing a broad range of rod separations, orientations, and aspect ratios. In short, to the best of our knowledge, a comprehensive model is not available to quantify for rods near walls how all the components of the diffusivity tensor, \mathbf{D} (and the resistance tensor, \mathbf{R} , via $\mathbf{D} = k\mathbf{TR}^{-1}$), depend on all possible rod configurations and aspect ratios. By obtaining such a model, it will be possible to accurately simulate and analyze rods near surfaces in terms of translational and rotational diffusivities as well as translational and rotational velocities due to external forces and torques.

One approach to compute \mathbf{D} is Stokesian dynamics,²⁷ which is the method employed in this work. Although Stokesian dynamics is often applied to problems in suspension rheology, it has been used successfully in bulk chain-of-sphere models to produce agreement with slender body theory,²⁸ as

^{a)} Author to whom correspondence should be addressed: mabevan@jhu.edu

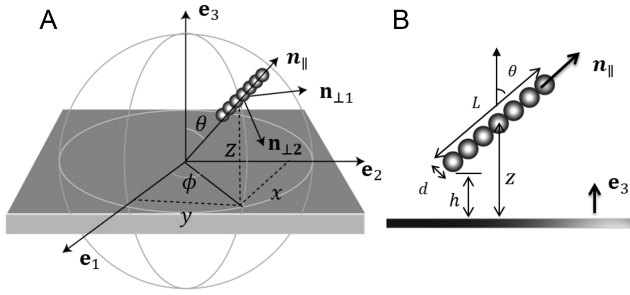


FIG. 1. Schematics of “chain-of-spheres” colloidal rod above the wall. (a) 3D view and (b) side view looking along $\mathbf{n}_{\perp 1}$. In both schematics, \mathbf{e}_1 , \mathbf{e}_2 , and \mathbf{e}_3 are unit vectors in a Cartesian coordinate lab frame, and $\mathbf{n}_{||}$, $\mathbf{n}_{\perp 1}$, and $\mathbf{n}_{\perp 2}$ are unit vectors in spherical coordinates in the particle frame with origin located at the rod center of mass.

well as spherical particles near surfaces^{9,29} and in confinement.¹⁰ In this work, we implement a Constrained Stokesian Dynamics (CSD) method to compute \mathbf{D} using a constraint strategy³⁰ to maintain a rigid linear chain-of-spheres as they interact with a wall. The CSD approach allows accurate modeling of chains-of-spheres to include both non-conservative hydrodynamic forces and conservative forces such as electrostatic and gravitational interactions.

In this work, we compute diffusivities for colloidal rods by modeling them as rigid chains-of-spheres in bulk media and near walls (Fig. 1) vs. aspect ratio, separation, and orientation. The theory, results, and their discussion are based on the systematic approach to compute diffusion coefficients, use these to perform dynamic simulations, and obtain diffusivities by analyzing trajectories (as they would be in experiments). In more detail, the paper is organized as follows. Translational and rotational components of \mathbf{D} are calculated using CSD for chain-of-sphere rods in bulk media for aspect ratios of $p=2$ -30. This approach is extended to chain-of-sphere rods near walls where separation dependent components of \mathbf{D} are calculated for parallel, perpendicular, and oblique orientations including translation, rotation, and translation-rotation cross terms. Dynamic simulations using the calculated \mathbf{D} are analyzed using mean squared positional and angular displacements and autocorrelation functions. These results are used to show how experimentally measured diffusivities can be quantitatively connected to components of \mathbf{D} and the conservative forces acting on rods near surfaces. Finally, the crossover from anisotropic to isotropic diffusion in bulk media and near walls is quantified from measured trajectories and shown to agree with theoretical predictions developed in this paper.

II. THEORY

A. Resistance, mobility, and diffusion coefficients

1. Coordinate systems

The following analysis uses two coordinate frames: a lab frame and a particle frame. As illustrated in Fig. 1, the lab frame is a right-hand Cartesian coordinate system with basis vectors $\mathbf{e}_1 = (1, 0, 0)$, $\mathbf{e}_2 = (0, 1, 0)$, and $\mathbf{e}_3 = (0, 0, 1)$. The particle frame is a right-hand Cartesian coordinate system with the origin at the rod center of mass with axis directions relative to

the rod long axis; specifically, $\mathbf{n}_{||}$ is the unit vector parallel to the rod long axis, $\mathbf{n}_{\perp 1}$ is perpendicular to $\mathbf{n}_{||}$ and \mathbf{e}_3 , and $\mathbf{n}_{\perp 2}$ is perpendicular to $\mathbf{n}_{||}$ and $\mathbf{n}_{\perp 1}$. The particle frame is translated and rotated relative to the lab frame with a polar angle θ and azimuthal angle ϕ .

2. Unbounded sphere resistance and mobility tensor

For N spheres of radius a suspended in an unbounded incompressible Newtonian fluid in the low Reynolds number limit, the equation of motion is given by

$$\mathbf{U} = \mathbf{M}\mathbf{F}, \quad (1)$$

where \mathbf{U} is the concatenation of translational and rotational velocity vectors of N spheres, $\mathbf{U} = (\mathbf{U}^{(1)}, \mathbf{U}^{(2)}, \dots, \mathbf{U}^{(N)})$, \mathbf{F} is the concatenation of forces and torques acting on the spheres, $\mathbf{F} = (\mathbf{F}^{(1)}, \mathbf{F}^{(2)}, \dots, \mathbf{F}^{(N)})$, where the superscript denotes the index of individual spheres, and \mathbf{M} is the grand mobility tensor of size $6N \times 6N$. The corresponding resistance relationship is given as

$$\mathbf{F} = \mathbf{R}\mathbf{U}, \quad (2)$$

where \mathbf{R} is the grand resistance tensor and relates to the grand mobility tensor as

$$\mathbf{R} = \mathbf{M}^{-1} \quad (3)$$

which can be computed using²⁷

$$\mathbf{R} = (\mathbf{M}_{\text{pp}}^{\infty})^{-1} + \mathbf{R}_{2\text{B}} - \mathbf{R}_{2\text{B}}^{\infty}, \quad (4)$$

which includes both far-field multi-body interactions [i.e., $(\mathbf{M}_{\text{pp}}^{\infty})^{-1}$] and near-field pair-wise lubrication (i.e., $\mathbf{R}_{2\text{B}}$). The far-field pairwise resistance (i.e., $\mathbf{R}_{2\text{B}}^{\infty}$) is subtracted since the far-field two-body interaction is already accounted for in $(\mathbf{M}_{\text{pp}}^{\infty})^{-1}$. Details of these expressions are included in the [supplementary material](#).

3. Sphere-wall resistance and mobility tensor

The grand resistance tensor for spheres above a planar no-slip wall is given as^{9,29}

$$\mathbf{R} = (\mathbf{M}_{\text{pw}}^{\infty})^{-1} + \mathbf{R}_{2\text{B}} + \mathbf{R}_{\text{W}} - (\mathbf{R}_{2\text{B},\infty} + \mathbf{R}_{\text{W},\infty}), \quad (5)$$

which includes both the multi-body far-field resistance tensor above a no-slip plane [i.e., $(\mathbf{M}_{\text{pw}}^{\infty})^{-1}$], which is the inversion of many-bodied far-field mobility tensor, and pair-wise lubrication interactions. The pair-wise lubrication interaction is obtained by first adding the two-body particle-particle exact resistance tensor $\mathbf{R}_{2\text{B}}$ and the particle-wall exact resistance tensor \mathbf{R}_{W} , and then subtracting the far-field resistance tensor $\mathbf{R}_{2\text{B},\infty} + \mathbf{R}_{\text{W},\infty}$ to avoid the double counting of the far-field particle-particle and particle-wall interaction in $(\mathbf{M}_{\text{pw}}^{\infty})^{-1}$ and $\mathbf{R}_{2\text{B}} + \mathbf{R}_{\text{W}}$. The elements in $\mathbf{R}_{2\text{B}}$ and $\mathbf{R}_{2\text{B}}^{\infty}$ are the same as Eq. (4). The explicit expressions for $(\mathbf{M}_{\text{pw}}^{\infty})^{-1}$ can be found in Ref. 29. Details of these expressions are included in the [supplementary material](#).

4. Chains-of-spheres-wall resistance and mobility tensor

We model rod-like particles as linear chains of touching spheres as depicted in Fig. 1. To model rod motion, the system is constrained to have six degrees of freedom (3 for translation and 3 for rotation). The rigid rod motion can be decomposed

into three degrees of translational motion of the center of mass and three degrees of rotational motion about the center of mass given by

$$\begin{pmatrix} \mathbf{F}_{rod} \\ \mathbf{L}_{rod} \end{pmatrix} = \mathbf{R}_{rod} \begin{pmatrix} \mathbf{U}_{rod} \\ \mathbf{\Omega}_{rod} \end{pmatrix}. \quad (6)$$

All quantities in Eq. (6) are calculated and measured in the particle frame. \mathbf{R}_{rod} is a 6×6 resistance tensor for the six degrees of freedom of a single rod. The entries in \mathbf{R}_{rod} can be calculated from Eqs. (2) and (6) by setting appropriate velocities to each sphere composing the rod. For example, if all spheres translate with unit velocity in the $\mathbf{n}_{||}$ direction, then Eq. (2) can be used to calculate the $6N$ dimensional vector of forces and torques acting on the individual spheres. Those forces and torques can be converted to a 3-dimensional force \mathbf{F}_{rod} and a 3 dimensional torque \mathbf{L}_{rod} acting on the rod relative to its center of mass. Since the rod translates with velocity vector $\mathbf{U}_{rod} = (1,0,0)$ and zero rotational velocity $\mathbf{\Omega}_{rod} = (0,0,0)$, the first row elements in \mathbf{R}_{rod} can be calculated by solving linear equations within Eq. (6). Other row elements in \mathbf{R}_{rod} are calculated in the same scheme. The diffusivity tensor \mathbf{D}_{rod} in the particle frame is related to \mathbf{R}_{rod} by

$$\mathbf{D}_{rod} = k_B T (\mathbf{R}_{rod})^{-1}. \quad (7)$$

The diagonal components in \mathbf{D}_{rod} are denoted as $D_{||}^{t,b}, D_{\perp 1}^{t,b}, D_{\perp 2}^{t,b}, D_{||}^{r,b}, D_{\perp 1}^{r,b}, D_{\perp 2}^{r,b}$ to represent primary translational and three rotational diffusivities along $\mathbf{n}_{||}$, $\mathbf{n}_{\perp 1}$, and $\mathbf{n}_{\perp 2}$. Off-diagonal elements of \mathbf{D}_{rod} are zero for bulk diffusion. A nearby wall introduces additional hydrodynamic interactions [i.e., Eq. (5)] for each sphere within the chain of spheres making up the rod particle. For interfacial diffusion, the diagonal components in \mathbf{D}_{rod} are denoted as $D_{||}^{t,w}, D_{\perp 1}^{t,w}, D_{\perp 2}^{t,w}, D_{||}^{r,w}, D_{\perp 1}^{r,w}, D_{\perp 2}^{r,w}$ to represent primary translational and rotational diffusivities in the similar to bulk diffusion modes. Off-diagonal terms in \mathbf{D}_{rod} are non-zero in the presence of the wall.

B. Equation of motion for dynamic simulations

1. Equation of motion under constraint

For N identical particles with coordinates $\mathbf{q} = (q_1, q_2, \dots, q_{6N})$, including $3N$ positional coordinates $(x_1, y_1, z_1, \dots, x_N, y_N, z_N)$ and $3N$ rotational coordinates $(\alpha_1, \beta_1, \gamma_1, \dots, \alpha_N, \beta_N, \gamma_N)$, the equation of motion is

$$\frac{d\mathbf{q}}{dt} = \mathbf{U} = \mathbf{M} \cdot \mathbf{F}, \quad (8)$$

where \mathbf{U} is a $6N$ dimensional velocity vector including $3N$ translational velocities and $3N$ rotational velocities. \mathbf{M} is a $6N \times 6N$ grand mobility tensor obtained from the grand resistance tensor in Eq. (6) via $\mathbf{M} = (\mathbf{R})^{-1}$ (see the [supplementary material](#) for more details). \mathbf{F} is a $6N$ dimensional force vector including $3N$ forces and $3N$ torques acting on the center of each particle, which is given by the sum of conservative forces, \mathbf{F}^P , and Brownian forces, \mathbf{F}^B , as

$$\mathbf{F} = \mathbf{F}^P + \mathbf{F}^B. \quad (9)$$

To model rods as chains-of-spheres that move together as a rigid body, the equation of motion [Eq. (8)] is modified to include additional constraint forces, \mathbf{F}^C , as

$$\mathbf{F} = \mathbf{F}^P + \mathbf{F}^B + \mathbf{F}^C. \quad (10)$$

2. Conservative forces

The $6N$ dimensional force vector \mathbf{F}^P is the concatenation of $(\mathbf{F}_1^P, \mathbf{F}_2^P, \dots, \mathbf{F}_N^P, \mathbf{L}_1^P, \mathbf{L}_2^P, \dots, \mathbf{L}_N^P)$, where \mathbf{F}_i^P and \mathbf{L}_i^P represent the conservative force and torque experienced by sphere i . The system considered throughout this paper does not have conservative torques and $\mathbf{L}_i^P = 0$ (although constraining torques are included). The conservative forces on each sphere i composing the rod experience electrostatic forces and gravitation force¹⁰

$$\begin{aligned} \mathbf{F}_i^P &= \kappa B^{pw} \exp(-\kappa(z_i - a)) \mathbf{e}_3 \\ &+ \sum_{j \neq i} \kappa B^{pp} \exp(-\kappa \|\mathbf{r}_{ij}\|) \frac{\mathbf{r}_{ij}}{\|\mathbf{r}_{ij}\|} + m\mathbf{g}, \end{aligned} \quad (11)$$

where a is the radius of the sphere, z_i is the mass center height of the sphere, κ is the Debye length, B^{pw} is the pre-factor for electrostatic repulsion between the sphere and wall, B^{pp} is the pre-factor for electrostatic repulsion between spheres, \mathbf{r}_{ij} is the vector from mass center of particle i to mass center of particle j , m is the buoyant sphere mass, and \mathbf{g} is the acceleration due to gravity.

3. Constraint forces

The motion of a rod with aspect ratio p can be modeled by the motion of p spheres under two types of constraints: positional constraints and rotational constraints. The positional constraints are used to ensure that all the spheres are positioned in one line and each sphere is touching with its neighbors. The rotational constraints are that all the spheres can only rotate along the long axis of the rod with the same angular speed, whereas rotations perpendicular to the long axis are not allowed. The details of the constraints can be found in the [supplementary material](#), but we provide a brief outline of how the constraint forces, \mathbf{F}^C , are determined. The K constraints, C_μ , on the coordinates \mathbf{q} are given by³¹

$$C_\mu(q_1, q_2, \dots, q_{6N}) = 0, \quad \mu = 1, 2, \dots, K \quad (12)$$

such that each coordinate q_j will experience an extra constraint force given as^{30,31}

$$F_j^C = \sum_{\mu=1}^K \lambda_\mu \frac{\partial C_\mu}{\partial q_j}, \quad (13)$$

where λ_μ are obtained by imposing the condition that the K constraints should be satisfied during the simulation to yield

$$\frac{\partial C_\mu}{\partial t} = \sum_{j=1}^{6N} \frac{\partial C_\mu}{\partial q_j} U_j = 0, \quad \mu = 1, 2, \dots, K \quad (14)$$

such that λ in Eq. (13) can be solved from Eqs. (8), (10), and (14).

4. Brownian forces

The Brownian forces \mathbf{F}^B are obtained by first generating the regular Brownian force as

$$\langle \mathbf{F}^B \rangle = 0, \quad \langle \mathbf{F}^B \mathbf{F}^B \rangle = \frac{2k_B T}{\Delta t} \mathbf{R} \quad (15)$$

and then projecting the generated forces $\mathbf{F}^{B'}$ via

$$\mathbf{F}^B = \mathbf{P} \cdot \mathbf{F}^{B'}, P_{ij} = \delta_{ij} - \sum_{v=1}^K \sum_{\mu=1}^K \frac{\partial C_\mu}{\partial q_i} \left(\sum_{k=1}^{6N} \frac{\partial C_\mu}{\partial q_k} \frac{\partial C_v}{\partial q_k} \right)^{-1} \frac{\partial C_v}{\partial q_j} \quad (16)$$

such that Brownian forces will be locally tangent to the $6N-K$ hyper-surface defined by the K constraints.³¹ Please see the [supplementary material](#) for a detailed description.

5. Mid-point algorithm

With forces calculated, the mid-point algorithm is used to update the coordinate.³¹ Specifically, the initial velocity and mid-point coordinate are first calculated as

$$\mathbf{U}^0 = (\mathbf{R}^0)^{-1} \cdot (\mathbf{F}^{P,0} + \mathbf{F}^{B,0} + \mathbf{F}^{C,0}), \quad (17)$$

$$\mathbf{q}^* = \mathbf{q}^0 + \frac{1}{2} \mathbf{U}^0 \Delta t, \quad (18)$$

and then the intermediate velocity and final position are calculated,

$$\mathbf{U}^* = (\mathbf{R}^*)^{-1} \cdot (\mathbf{F}^{P,*} + \mathbf{F}^{B,*} + \mathbf{F}^{C,*}), \quad (19)$$

$$\mathbf{q} = \mathbf{q}^0 + \mathbf{U}^* \Delta t, \quad (20)$$

where Δt is the integration time, and “0” and “*” denote the quantity that is calculated using the initial and mid-point configurations, respectively.

C. Equilibrium and dynamic analyses of rod diffusion

1. Equilibrium rod-wall distribution

For a rod levitated above a wall in nearly quasi-2D configurations (with the long-axis parallel to the wall), we characterize its configuration by the center-of-mass coordinates (x, y, z) and the polar angle θ (there is no dependence on the azimuthal angle). The net potential energy of a rod is the sum of potential energies for each sphere within the rod given by

$$U_{rod}(z, \theta) = \sum_{i=1}^p G_s z_i + B^{pw} \exp[-\kappa(z_i - a)], \quad (21)$$

where G_s is the buoyant weight of each sphere, z_i is the mass center of particle i composing the rod and can be related to z and θ by

$$z_i = z + 2a \cos(\theta) [i - (1 + p/2)]. \quad (22)$$

The equilibrium probability of a rod is given by a Boltzmann distribution as

$$\rho^{eq}(z, \theta) = N_0 \sin(\theta) \exp[-U_{rod}(z, \theta)/k_B T], \quad (23)$$

where $\sin(\theta)$ is the factor accounting for the degeneracy when integrating out the variable of azimuth angle ϕ (there is no ϕ dependence), and N_0 is the normalizing factor to ensure the unit area for the integral of $\rho^{eq}(z, \theta)$. The effective energy landscape then becomes

$$\frac{W(z, \theta)}{k_B T} = -\ln[\rho^{eq}(z, \theta)] + C, \quad (24)$$

where C is an integration constant related to a reference energy. The 2D energy landscape that can be converted to 1D effective energy landscape in either coordinate by integration is

$$\begin{aligned} \frac{W_\theta(\theta)}{k_B T} &= \int \exp[-W_{rod}(z, \theta)/k_B T] dz + C, \\ \frac{W_z(z)}{k_B T} &= \int \exp[-W_{rod}(z, \theta)/k_B T] d\theta + C. \end{aligned} \quad (25)$$

2. Rod diffusion far from an interface

The anisotropic diffusion behavior of a rod-shaped particle can be characterized by the mean squared positional displacement (MSPD) along directions parallel and perpendicular to the long axis. The displacement vector of the center of mass at time t can be decomposed into parallel and perpendicular components based on the initial orientation in the particle frame (Fig. 1). For MSPDs in parallel and perpendicular directions (see the [supplementary material](#)),

$$\begin{aligned} \langle \Delta r_{\parallel}(t) \Delta r_{\parallel}(t) \rangle &= 2D'_{\perp 1} t + \frac{2}{3} (D'_{\parallel} - D'_{\perp 1}) t + \frac{4}{3} (D'_{\parallel} - D'_{\perp 1}) \\ &\quad \times \frac{1}{6D'_{\perp 1}} [1 - \exp(-6D'_{\perp 1} t)], \\ \langle \Delta r_{\perp 1}(t) \Delta r_{\perp 1}(t) \rangle &= 2D'_{\perp 1} t + \frac{2}{3} (D'_{\parallel} - D'_{\perp 1}) t - \frac{2}{3} (D'_{\parallel} - D'_{\perp 1}) \\ &\quad \times \frac{1}{6D'_{\perp 1}} [1 - \exp(-6D'_{\perp 1} t)], \end{aligned} \quad (26)$$

where angle brackets indicate the ensemble average. For bulk diffusion, $\langle \Delta r_{\perp 1}(t) \Delta r_{\perp 1}(t) \rangle$ and $\langle \Delta r_{\perp 2}(t) \Delta r_{\perp 2}(t) \rangle$ are equivalent. If the MSPD is calculated by averaging over all trajectories with different initial orientations and all time scales, the results in Eq. (26) reduce to

$$\langle \Delta r(t) \Delta r(t) \rangle = 4D'_{\perp 1} t + 2D'_{\parallel} t, \quad (27)$$

where $(\Delta r)^2 = (\Delta r_{\parallel})^2 + (\Delta r_{\perp 1})^2 + (\Delta r_{\perp 2})^2$. 3D Brownian rotation is usually characterized by an orientation auto-correlation function related to rotational diffusivity as³²

$$\langle \mathbf{n}_{\parallel}(t) \cdot \mathbf{n}_{\parallel}(0) \rangle = \exp(-2D'_{\perp 1} t), \quad (28)$$

where $\mathbf{n}_{\parallel}(t)$ is the rod's orientation vector at an elapsed time, t .

3. Rod diffusion parallel to a wall

For rods adjacent to a wall, the 2D projected MSPD and mean squared angular displacements (MSADs) are measurable quantities to characterize rod diffusion. Assuming the rod is strictly moving in 2D, the parallel and perpendicular MSPDs [from Eq. (26)] become²¹

$$\begin{aligned} \langle \Delta r_{\parallel}(t) \Delta r_{\parallel}(t) \rangle &= (D'_{\parallel} + D'_{\perp 1}) t - (D'_{\perp 1} - D'_{\parallel}) \\ &\quad \times \frac{1}{4D'_{\perp 2}} [1 - \exp(-4D'_{\perp 2} t)], \\ \langle \Delta r_{\perp 1}(t) \Delta r_{\perp 1}(t) \rangle &= (D'_{\parallel} + D'_{\perp 1}) t + (D'_{\perp 1} - D'_{\parallel}) \\ &\quad \times \frac{1}{4D'_{\perp 2}} [1 - \exp(-4D'_{\perp 2} t)], \end{aligned} \quad (29)$$

and similar to Eq. (27) for bulk diffusion, the MSPD averaged over all orientations is

$$\langle \Delta r(t) \Delta r(t) \rangle = 2(D'_{\parallel} + D'_{\perp 1}) t. \quad (30)$$

In the event that z and θ are not strictly constrained, the projected 2D MSPD is obtained by replacing diffusivities in Eq. (29) with probability-weighted diffusivities as¹

$$\begin{aligned} \langle D_{\parallel}^t \rangle_{z,\theta} &= \int (D_{\parallel}^t \sin^2 \theta + D_{\perp 2}^t \cos^2 \theta) \rho^{eq}(z, \theta) d\theta dz, \\ \langle D_{\perp 1}^t \rangle_{z,\theta} &= \int D_{\perp 1}^t \rho^{eq}(z, \theta) d\theta dz, \end{aligned} \quad (31)$$

where subscripts denote averages over the indicated variables, where $\rho^{eq}(z, q)$ is the equilibrium distribution from Eq. (23).

4. Rod diffusion normal to wall

Rod diffusion normal to a wall is separation dependent via hydrodynamic interactions.^{13,33} Diffusion coefficients are connected to the normal-to-wall component in the MSPD as¹¹

$$D_3^t(z) = \frac{1}{2} \lim_{t \rightarrow 0} \frac{\langle (\Delta x_3(z, t))^2 \rangle}{t}, \quad (32)$$

which can be used to extract the diffusion coefficient from particle trajectories. The diffusion coefficients can also be related to diffusion coefficients in the particle frame as

$$D_3^t(z) = \int (D_{\parallel}^t \cos^2 \theta + D_{\perp 2}^t \sin^2 \theta) \rho^{eq}(\theta) d\theta. \quad (33)$$

III. METHODS

We implemented CSD for two types of experiments: rod diffusion in bulk media and near a wall. In both cases, the rod material properties correspond to gold (Au) nano-rods of different aspects in aqueous media with 0.1 mM univalent electrolyte ($G_s/a = 0.297kT$, $B^{pw} = 486.6kT$, $\kappa^{-1} = 30$ nm) with the forces listed in the [supplementary material](#). In both cases, the spheres composing the rod have a radius of $a = 200$ nm. For bulk diffusion, the rod aspect ratio is $p = 4$, rods are only subject to Brownian forces, the integration time step is 0.5 ms, and particle coordinates are recorded every 50 steps for 10 000 s. For rods adjacent to walls, rod aspect ratios include $p = 4, 7, 12$, and rods are subject to gravitational, electrostatic, and Brownian forces. For the rod-wall cases, the integration time step is 0.2 ms and particle coordinates are recorded every 50 steps for 2000 s. Boltzmann inversions of time averaged particle distributions [Eqs. (24) and (25)] are used to obtain energy landscapes from simulated trajectories. The vertical position, z , and polar angle, θ , are discretized with a resolution of 20 nm and 1° . For dynamic analyses, time-resolved MSPD and orientation auto-correlation function are calculated from simulated trajectories.

IV. RESULTS AND DISCUSSION

A. Rod bulk diffusivities

Figure 2 depicts the bulk diffusion modes for rods with aspect ratios of $p = 2$ -30 calculated via the CSD method and its comparison with cylindrical rod results.¹⁸ For a single rod far from any boundaries, off-diagonal terms of \mathbf{D}_{rod} in the particle frame vanish since there are no correlations between different types of motion. In the bulk, translational and rotational diffusivities along $\mathbf{n}_{\perp 1}$ and $\mathbf{n}_{\perp 2}$ are equivalent, so results

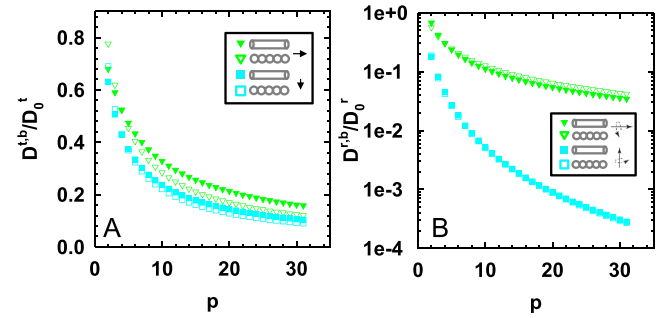


FIG. 2. Bulk diffusivities for chain-of-spheres vs. cylinders vs. aspect ratio ($p = 2$ -30). (a) Translational diffusivities (normalized by $kT/6\pi\mu a$) along \mathbf{n}_{\parallel} (green) for chain-of-spheres (open triangle) vs. cylinder model (filled triangles) and along $\mathbf{n}_{\perp 1}$ (cyan) for chain-of-spheres (open squares) vs. cylinder model (filled squares). (b) Rotational diffusivities (normalized by $kT/8\pi\mu a^3$) about \mathbf{n}_{\parallel} (green) for chain-of-spheres (open triangle) vs. cylinder model (filled triangles) and about $\mathbf{n}_{\perp 1}$ (cyan) for chain-of-spheres (open squares) vs. cylinder model (filled squares).

are only shown for $\mathbf{n}_{\perp 1}$. In Fig. 2(a), translational diffusivities along $\mathbf{n}_{\perp 1}$ for chains-of-spheres show a systematic positive deviation ($<10\%$) from the cylinder model for $p > 3$. The positive deviation can be understood through the fact that when a sphere translates through a quiescent flow, it experienced less drag than a cylindrical surface of length $2a$ translating perpendicular to its axis.

For translational diffusion along \mathbf{n}_{\parallel} , the chain-of-spheres model yields an overall smaller value ($<20\%$) than the cylinder model. The cylinder model¹⁸ is based on using many small spherical beads to model the cylinder shape. As such, it appears that the translational diffusivity along \mathbf{n}_{\parallel} in the cylinder model is greater than the chain-of-spheres model because the density of smaller spherical beads composing the rod surface makes the cylinder smoother. Therefore, the difference is due to the finite size effect of the spheres in the chain-of-sphere rod, with the chain of spheres providing more friction as a corrugated surface.

In Fig. 2(b), we observed a close correspondence ($<5\%$) between the two models for rotational diffusivities about $\mathbf{n}_{\perp 1}$. However, the rotational diffusivity about \mathbf{n}_{\parallel} shows higher diffusivities for the chain-of-spheres computed to the cylinder model ($<20\%$, difficult to see on the log scale). The reason for this discrepancy is likely the same as in the case of translation along \mathbf{n}_{\parallel} ; the rotation of spheres experiences less drag than the rotation of a short cylindrical surface section of length $2a$. For convenience and ease of use of the theoretical results in Fig. 2, empirical fits to length and aspect ratio dependent bulk diffusivities, $D(L, p)$, are reported in the [supplementary material](#) with a general form with coefficients a_i given by

$$D(L, p) = \frac{kT}{2\pi\mu L} \left[\ln p + \frac{a_1 p^2 + a_2 p + a_3}{p^2 + a_4 p + a_5} \right]. \quad (34)$$

B. Rod diffusivity near a wall

Figure 3 depicts height-dependent diffusivities for rods consisting of chains-of-spheres parallel to a wall for $p = 7, 12$. Each diffusivity is normalized by its bulk value so that all values approach zero as particle-wall surface separation, h , vanishes and unity as separation becomes large ($>50a$).

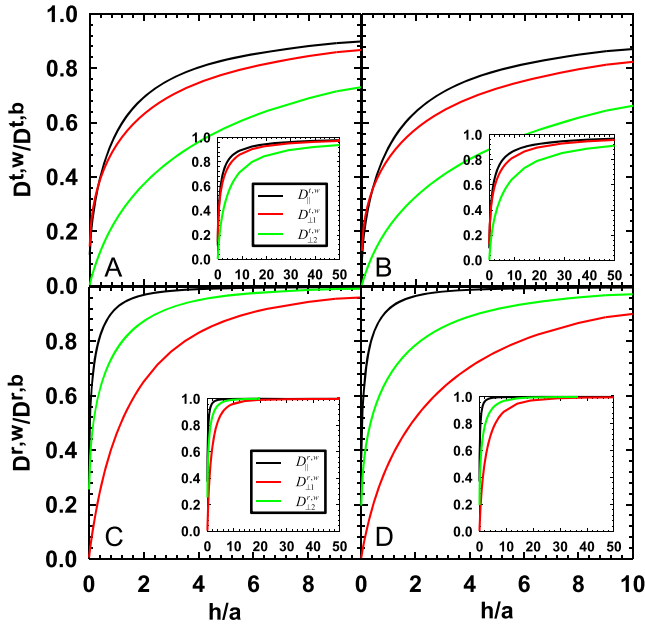


FIG. 3. Diffusivities for chain-of-spheres rod oriented parallel to wall. Height dependent coefficients in directions \mathbf{n}_{\parallel} (black), $\mathbf{n}_{\perp 1}$ (red), $\mathbf{n}_{\perp 2}$ (green) for translational diffusivities of rods with aspect ratios (a) $p = 7$, (b) $p = 12$ and for rotational diffusivities with aspect ratios (c) $p = 7$, (d) $p = 12$.

Figure 3(a) shows translational diffusivities in the three directions each having a distinct elevation and aspect ratio dependence. Translational diffusivities for the chain-of-spheres follow trends for a single sphere approaching a wall.¹³ All diffusivities decrease with decreasing separation, even when $h/a \sim 50$, which reflects far-field hydrodynamic interactions. Translational diffusivity decreases fastest along $\mathbf{n}_{\perp 2}$ as $O(h/a)$ and more slowly along \mathbf{n}_{\parallel} and $\mathbf{n}_{\perp 1}$ as $O(\ln(h/a))$.

The hydrodynamic hindrance increases for longer rods. For chains-of-spheres above a wall, the contribution of each sphere to increasing drag can be understood by the addition of 2-body hydrodynamic interactions as well as multi-body interactions between particles and the wall. The increasing drag per unit length becomes smaller as the rod length increases ($p > 20$) since multi-body interactions between distant neighbors eventually become insignificant. Effects of multi-body hydrodynamics are most pronounced at intermediate separations ($1 < h/a < 10$). In the far-field ($h/a > 10$) and in the lubrication ($h/a \ll 1$) limits, the net interaction is dominated by pairwise interactions of the wall with each sphere within the chain-of-spheres.

Height dependent rotational diffusivities in the three directions are shown in Figs. 3(c) and 3(d). Rotations about $\mathbf{n}_{\perp 1}$ and $\mathbf{n}_{\perp 2}$ experience wall interactions when $h \approx 20-30a$, whereas rotation about \mathbf{n}_{\parallel} begins to deviate from bulk behavior for $h < 5a$. Although chain-of-sphere translation and rotation about $\mathbf{n}_{\perp 1}$ and $\mathbf{n}_{\perp 2}$ both involve translation of constituent spheres in the $\mathbf{n}_{\perp 1}$ and $\mathbf{n}_{\perp 2}$ directions, rotational hindrance is shorter-ranged compared to translational hindrance. This can be understood by considering the wall effect on the collective motion of spheres comprising the chain-of-spheres. Consider one sphere translating in bulk and generating a flow field along the translation direction; a nearby sphere will experience a higher mobility when it translates in the same direction and

a lower mobility when translating in the opposite direction. When two spheres are near a wall, a no-slip boundary changes the flow field so that mobilities associated with collective motion decrease compared to the bulk, and mobilities for relative motion increase compared to the bulk (see hydrodynamic screening due to no-slip boundaries discussed elsewhere³⁴). For translations along \mathbf{n}_{\parallel} , $\mathbf{n}_{\perp 1}$, and $\mathbf{n}_{\perp 2}$, all spheres move in the same direction, and the wall exerts a long-range hindrance. For rotations about $\mathbf{n}_{\perp 1}$ and $\mathbf{n}_{\perp 2}$, half the spheres move in the opposite direction to the other half; thus, the wall exerts a relatively weaker and short-ranged hindrance.

For rods much closer to the wall, near-field effects dominate a dramatic drop in diffusivities as they vanish near contact similar to the translational diffusivity. There are several interesting features in the height dependence of different rotational diffusivity modes. The rotation about $\mathbf{n}_{\perp 1}$ decreases faster than rotation about $\mathbf{n}_{\perp 2}$ since rotation about $\mathbf{n}_{\perp 1}$ involves translation of spheres normal to the wall. In the lubrication limit, rotation about \mathbf{n}_{\parallel} and $\mathbf{n}_{\perp 2}$ vanishes slower as $O(\ln(h/a))$ but rotation about $\mathbf{n}_{\perp 1}$ vanishes faster as $O(h/a)$. The rotational diffusion along the \mathbf{n}_{\parallel} direction generally has smaller and shorter-ranged interactions compared to other modes because the decrease of rotational diffusivity of constituent spheres along the \mathbf{n}_{\parallel} direction scales as $(h/a)^3$ whereas the decrease of the translational diffusivity of constituent spheres scales as (h/a) .³⁵

To practically implement the theoretical results reported in Fig. 3, empirical fits are reported in the [supplementary material](#). To illustrate the form of these corrections for a particular case, the correction for rod diffusion parallel to a wall is given by

$$f_{\parallel,p}^t(h) = \frac{D_{\parallel}^{t,w}(L,p,h)}{D_{\parallel}^{t,b}(L,p)}, \quad (35)$$

where both terms on the right hand side are given by Eq. (7). Based on this definition, Eq. (35) approaches 1 as h approaches infinity and 0 as h vanishes. The fit form of $f(h)$ is

$$f_{\parallel}^t(h) = \frac{a_1(h/a) + a_2(h/a)^2 + a_3(h/a)^3}{1 + a_4(h/a) + a_5(h/a)^2}, \quad (36)$$

where a_i are fitting coefficients. When $a < h < 10a$, an additional function [denoted as $g(p)$ in the [supplementary material](#)] is required to account for an additional weak aspect ratio dependence beyond the bulk dependence. As explained in more detail in the [supplementary material](#), it is possible to compute all diffusivities with a general form given by $D(L,p,h) = D(L,p)f(h)g(p)$.

C. Translational and rotational coupling

In contrast with bulk diffusion, rod particles near surfaces have coupling between translational and rotational modes, which is captured by non-zero, off-diagonal terms in the diffusivity tensor. To characterize coupling, we define a correlation coefficient as

$$\text{Corr}_{ij} = D_{ij} / \sqrt{D_{ii}D_{jj}}, \quad (37)$$

where i and j have indices, T $_{\parallel}$, T $_{\perp 1}$, T $_{\perp 2}$ representing translation along \mathbf{n}_{\parallel} , $\mathbf{n}_{\perp 1}$, $\mathbf{n}_{\perp 2}$, and R $_{\parallel}$, R $_{\perp 1}$, R $_{\perp 2}$ representing rotation about \mathbf{n}_{\parallel} , $\mathbf{n}_{\perp 1}$, $\mathbf{n}_{\perp 2}$.

In Fig. 3 where the rod is parallel to a wall, the symmetric nature of this configuration produces little coupling, although some weak coupling exists between translation along $\mathbf{n}_{||}$ and rotation about $\mathbf{n}_{\perp 1}$. To consider coupling in a more interesting configuration, Fig. 4 shows results for a rod of aspect ratio $p = 7$ at $\theta = 45^\circ$ angle (i.e., angle between $\mathbf{n}_{||}$ and \mathbf{e}_3 is 45°). Figures 4(a) and 4(b) show the diagonal terms of \mathbf{D} vs. the distance of the closest approach between the lowest sphere and the wall, h . As the rod-wall separation decreases, all diffusive modes decrease monotonically similar to the overall trend for rods oriented parallel to a wall in Fig. 3. However, the exact coefficients have different functional forms. For example, translational diffusivities decrease faster than the parallel case because the motion along $\mathbf{n}_{||}$ involves components of motion normal to the wall.

The translation-rotation coupling of rods near surfaces shows several interesting effects. Figure 4(c) shows height dependent correlation coefficients ($Corr_{T||,T\perp 2}$, $Corr_{T||,R\perp 1}$, $Corr_{T\perp 1,R\perp 2}$, $Corr_{T\perp 2,R\perp 1}$) from Eq. (37) for off-diagonal/coupling terms in the diffusivity tensor. For example, the terms $Corr_{T||,T\perp 2}$ and $Corr_{T||,R\perp 1}$ show how translation along $\mathbf{n}_{||}$ induces translation along $\mathbf{n}_{\perp 2}$ and rotation about $\mathbf{n}_{\perp 1}$ [Figs. 4(e) and 4(f)]. This has the net effect of the rod aligning itself with the wall and having an apparent attraction to the wall. As such, the rod moves a shorter distance compared to the case without coupling where only translation along $\mathbf{n}_{||}$ is allowed.³⁶ In another case, coupling $Corr_{T\perp 1,R\perp 2}$ between translation along $\mathbf{n}_{\perp 1}$ with rotation about $\mathbf{n}_{\perp 2}$ [Fig. 4(g)] is due to non-uniform drag on the rod by the wall; lower end

experiences more drag than the upper end. As such, when a lateral force is applied along $\mathbf{n}_{\perp 1}$, the upper end tends to move faster than the lower end and consequently the rod rotates. Similar reasoning applies to the coupling $Corr_{T\perp 2,R\perp 1}$ between translation in $\mathbf{n}_{\perp 2}$ and rotation about $\mathbf{n}_{\perp 1}$ [Fig. 4(h)]. All correlation coefficients become non-negligible for $h/a < 1$.

In Fig. 4(d), we investigate the angular dependence of correlation coefficients at fixed separation, $h/a = 0.05$. The coupling $Corr_{T||,T\perp 2}$ of translation along $\mathbf{n}_{||}$ with translation about $\mathbf{n}_{\perp 2}$ [Fig. 4(e)] has a maximum at $\sim 30^\circ$ and vanishes at both normal and parallel configurations. Similarly, the coupling of $Corr_{T||,R\perp 1}$ translation along $\mathbf{n}_{||}$ with rotation about $\mathbf{n}_{\perp 1}$ [Fig. 4(f)] is a maximum at $\sim 30^\circ$ and vanishes at both normal and parallel configurations. The coupling $Corr_{T\perp 1,R\perp 2}$ between translation along $\mathbf{n}_{\perp 1}$ and rotation about $\mathbf{n}_{\perp 2}$ [Fig. 4(g)] decreases monotonically from the normal configuration ($\theta = 0^\circ$), where the imbalance of drag between the two ends is greatest, to the parallel configuration ($\theta = 90^\circ$), where the imbalance disappears. For the coupling $Corr_{T\perp 2,R\perp 1}$ between translation along $\mathbf{n}_{\perp 2}$ and rotation about $\mathbf{n}_{\perp 1}$ [Fig. 4(h)], the correlation somewhat surprisingly peaks at $\sim 80^\circ$. This arises from the reverse upward fluid flow when particles are moving towards a wall that induces a rotation about $\mathbf{n}_{\perp 1}$. Due to symmetry, there is no coupling between (1) translations along $\mathbf{n}_{||}$ with translation along $\mathbf{n}_{\perp 1}$, (2) translation along $\mathbf{n}_{||}$ with rotation about $\mathbf{n}_{||}$, and (3) translation along $\mathbf{n}_{\perp 2}$ with rotation about $\mathbf{n}_{||}$.

D. Analysis of bulk rod diffusion

With the ability to predict \mathbf{D} , dynamic simulations using \mathbf{D} are used to show how analysis of rod trajectories, as in microscopy experiments, can be used to measure and model diffusion with connections to components of \mathbf{D} . Figure 5 reports results of the analysis of bulk diffusion trajectories of a single rod with $p = 5$. CSD was used to produce simulated random walk trajectories in bulk media [Fig. 5(a)] by considering only Brownian forces in Eq. (17). Vectors schematically depicted in Fig. 5(a) show how each three dimensional translational step in the lab frame is decomposed into components parallel and perpendicular to the rod axis in the particle frame. Figure 5(b) shows MSPD curves generated from simulated trajectories. Results in Fig. 5(b) include an MSPD for the center of mass in the lab frame as well as MSPDs parallel and perpendicular to the rod long axis in the particle frame. MSPD curves measured from simulated trajectories show agreement with theoretical predictions in Eqs. (26) and (27) for diffusion in the particle and laboratory frames.

The rotational diffusion characteristic time, $\tau_c = 1/2D'_{\perp 2}$, captures the process of losing directional memory and the crossover from anisotropic translational diffusion to isotropic translational diffusion. In the short time limit ($t \ll \tau_c$), the anisotropic translational diffusion behavior is demonstrated by fast and slow MSPD curves in parallel (i.e., $\mathbf{n}_{||}$ direction) and perpendicular (i.e., $\mathbf{n}_{\perp 1}$ direction) directions. For $t > \tau_c$, the two curves [represented in Eq. (29)] converge towards one curve [given by $(D'_{||} + D'_{\perp 1})t$, see Eq. (27)], indicating the transition from anisotropic to isotropic diffusion. Figure 5(c)

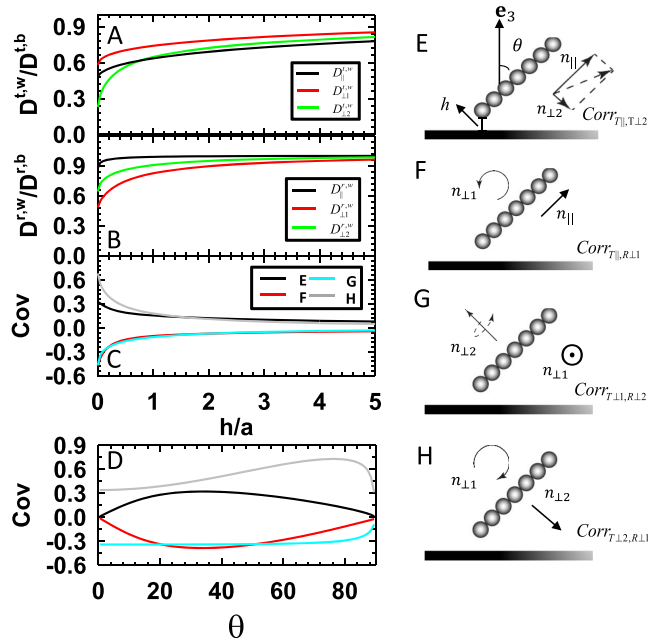


FIG. 4. Chain-of-spheres oblique ($\phi = 45^\circ$) to the wall for $p = 7$. Height (distance of the closest approach) dependent coefficients for (a) translational and (b) rotational diffusivities along/about $\mathbf{n}_{||}$ (black), $\mathbf{n}_{\perp 1}$ (red), and $\mathbf{n}_{\perp 2}$ (green). (c) Height and (d) angle dependent correlation coefficients [Eq. (37)] for coupled motions including (e) translation along $\mathbf{n}_{||}$ and translation along $\mathbf{n}_{\perp 2}$ ($Corr_{T||,T\perp 2}$, black), (f) translation along $\mathbf{n}_{||}$ and rotation about $\mathbf{n}_{\perp 1}$ ($Corr_{T||,R\perp 1}$, red), (g) translation along $\mathbf{n}_{\perp 1}$ and rotation about $\mathbf{n}_{\perp 2}$ ($Corr_{T\perp 1,R\perp 2}$, cyan), (h) translation along $\mathbf{n}_{\perp 2}$ and rotation about $\mathbf{n}_{\perp 1}$ ($Corr_{T\perp 2,R\perp 1}$, gray).

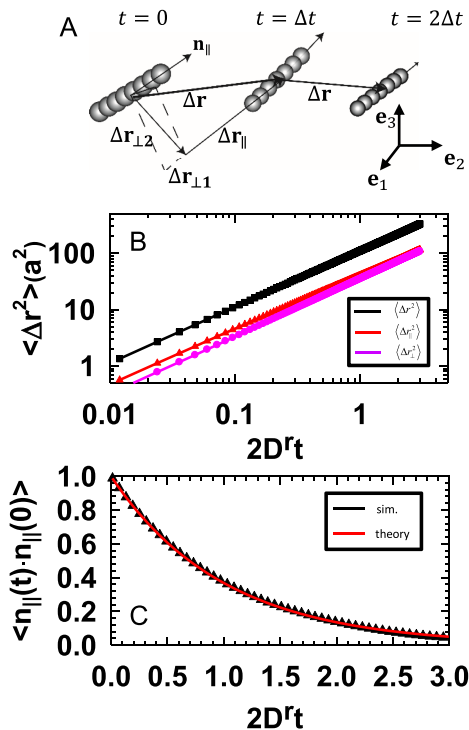


FIG. 5. MSPD and orientation autocorrelation function for bulk rod diffusion for $p = 5$. (a) Schematic of the rod trajectory with displacement vector $\Delta \mathbf{r}$ decomposed into components parallel and perpendicular to the rod axis in the particle frame with unit vectors in the lab frame shown for reference. (b) MSPD from simulation (points) vs. theory [Eqs. (26) and (27)] (lines) for translational diffusion (black) in the lab frame, (red) parallel to the rod long axis in the particle frame, and (pink) perpendicular to the rod long axis in the particle frame. (c) Orientation autocorrelation function from simulation (black triangles) and theory [Eq. (28)] (red line).

shows the orientation autocorrelation function calculated from simulation trajectories and the theoretical prediction from the right hand side of Eq. (28) [using D_r from Eq. (7)]. Excellent

agreement is observed between measured simulation results and theoretical predictions. The autocorrelation function confirms rods lose orientational correlation on the characteristic time scale τ_c .

E. Analysis of rod diffusion near a wall

The simulations and analyses of bulk rod diffusion are extended here to rods near walls. Because dynamic analyses require information on how rod states are sampled near surfaces, our results first quantify time-averaged equilibrium distributions of rod elevation and orientation. Figure 6 shows equilibrium distributions of rods with $p = 4, 7, 12$ confined near a wall surface by gravity (normal to the underlying wall) while experiencing electrostatic repulsion. In particular, CSD simulations are performed with rods subject to gravitational, electrostatic, and Brownian forces. Energy landscapes parameterized by the rod elevation and azimuthal angle (z, θ) are used to characterize equilibrium distribution of states.

As shown in Figs. 6(a)–6(f), 2D energy landscapes from predictions [Eqs. (21)–(25)] and measured from simulations [via Boltzmann inversion, Eqs. (24) and (25)] show good agreement. For rods of all lengths, the most probable configuration is aligned parallel to the wall ($\theta = 90^\circ$). Longer rods are more constrained in both z and θ . At the same height, longer rods are more constrained in θ due to electrostatic repulsion from the wall. In addition, longer rods are more constrained in z due to their increasing buoyant weight. Results in Figs. 6(g) and 6(h) also show projected one-dimensional energy landscapes vs. z and θ using Eq. (25). As p increases, the region of low energy/frequent sampling ($W < 5kT$) in height z is reduced from $\sim 6a$ to $\sim 2a$. With regard to orientation dependence, a rod with $p = 4$ has a non-vanishing probability to be aligned normal to the interface ($\theta = 0^\circ$), whereas a rod with

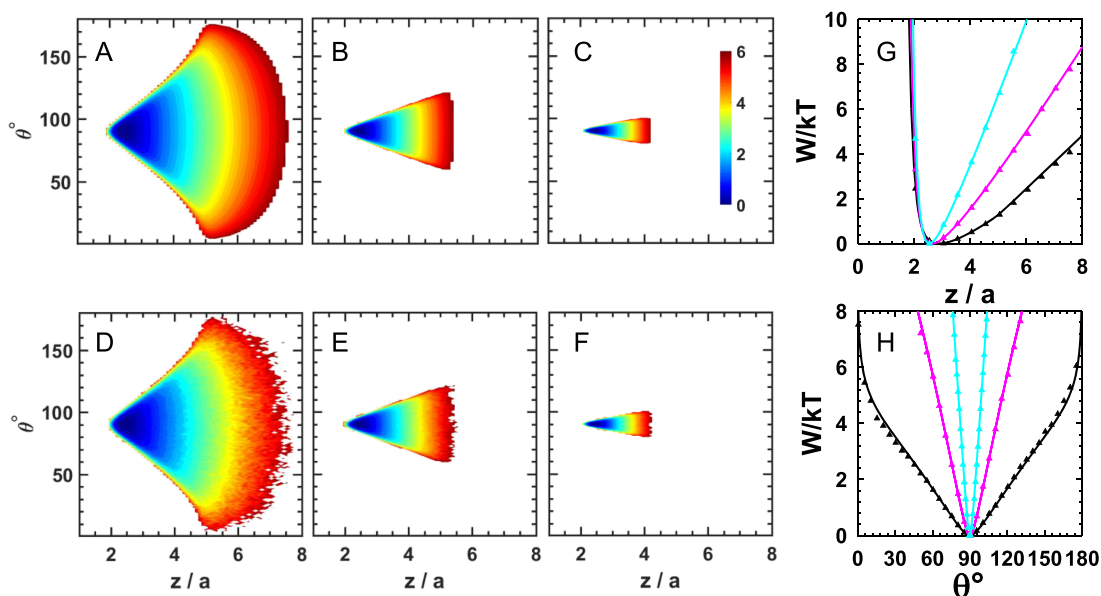


FIG. 6. Energy landscapes for a single rod above the wall for analyzing average diffusivities [via Eqs. (31) and (33), see Fig. 7]. For rods with $p = 4, 7, 12$, two dimensional energy landscapes vs. elevation z/a and θ as predicted from Eq. (24) [(a)–(c)] and as measured from CSD simulations via an inverse Boltzmann analysis in Eq. (24) [(d)–(f)]. One dimensional energy landscapes vs. (g) z/a and (h) θ for the same rods in (a)–(f) plotted as (black) $p = 4$, (pink) $p = 7$, and (cyan) $p = 12$ with (symbols) simulation results and (lines) from Eq. (25).

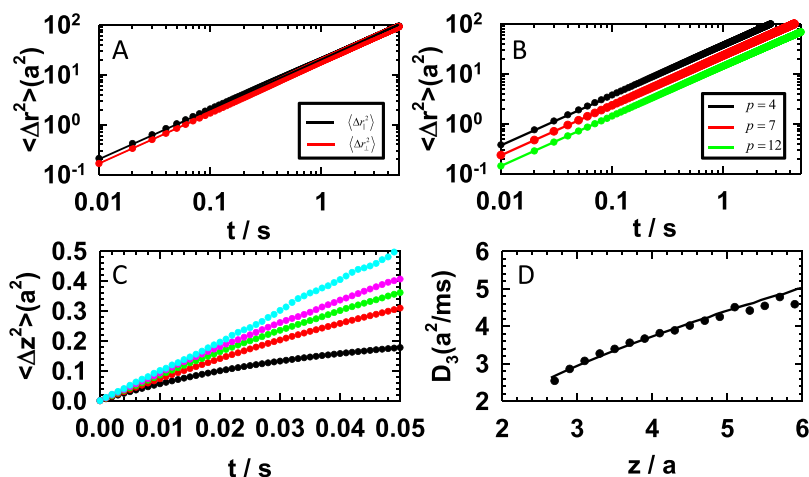


FIG. 7. Trajectory analysis for a single rod near a wall. (a) Rod with $p = 4$ near a wall for interactions in Fig. 6(a), MSPDs parallel (black) and perpendicular (red) to the rod long axis in the particle frame from simulated trajectory (symbols) and theory [lines, Eq. (29)]. (b) MSPDs for center of mass coordinates in the lab frame for rods with $p = 4$ (black), $p = 7$ (red), and $p = 12$ (green) from simulated trajectory [symbols, from Figs. 6(a)–6(f)] and theory [lines, Eq. (30)]. (c) MSPDs for center of mass for a rod with $p = 7$ [from Figs. 6(b) and 6(e)] normal to wall vs. elevation for starting coordinates at (bottom-to-top) $z = 2.9a, 3.9a, 4.9a, 5.9a, 6.9a$. (d) Normal particle-wall diffusivity vs. elevation [$D_3(z)$] from MSPDs in (c) via Eq. (32) (points) and theory in Eq. (33) (line).

$p = 12$ can only sample angles within $\pm 10^\circ$ of the parallel configuration.

For experiments where particle trajectories are measured adjacent to a wall, the MSPD is often used to quantify diffusion.²¹ Figure 7(a) shows 2D parallel and perpendicular components of the MSPD in the particle frame for a rod with aspect ratio 4 from the simulation and the theoretical curves from Eq. (29). Similar to 3D bulk translational diffusion, faster diffusion is observed along the rod long axis at short times until the crossover to isotropic diffusion occurs on the characteristic time scale for rotational diffusion. Figure 7(b) shows how translational diffusion parallel to the wall varies for $p = 4, 7$, and 12 . These data show that at longer times when diffusion is isotropic, higher aspect ratio rods have smaller average diffusivities as the result of their great size and their sampling lower elevations as the result of their greater buoyant weight.

Figure 7(c) shows diffusion normal to the wall for a rod with $p = 7$. The MSPDs are for different starting elevations¹¹ and show a systematic decrease as the rod elevation decreases. The decreasing diffusivity is due to increasing hydrodynamic hindrance as the rod is closer to the wall. As shown in Fig. 7(d), the diffusivities extracted from the initial slopes of the MSPD curves in Fig. 7(c) based on Eq. (32) have good agreement with theory prediction from Eq. (33). The significant change in diffusivity vs. elevation is similar to spheres¹³ and indicates that treating rod diffusivities as a constant when approaching a surface can produce significant errors when either interpreting measurements or predicting interfacial or confined rod particle dynamics.

V. CONCLUSION

Our results include methods to compute diffusivities, simulate dynamics, and analyze trajectories for colloidal rods in bulk media and near wall surfaces by modelling rods as chains-of-spheres. Diffusion coefficients and simulated trajectories are based on a constrained Stokesian dynamics method to include hydrodynamic interactions, whereas trajectory analyses are general to any anisotropic particle near a wall. Bulk diffusivities show good correspondence with established literature results, and diffusivities near walls are summarized in

terms of separation and aspect ratio dependent rational expressions fit to modeling results. Analyses of particle trajectories in terms of time-averaged equilibrium distribution functions and MSPDs show good agreement between measured quantities and theoretical predictions, including a crossover from anisotropic to isotropic translational diffusion. The methods reported in this work are sufficiently general that they should be readily extendable to other anisotropic particle shapes and many-particle concentrated systems near wall surfaces in future work.

SUPPLEMENTARY MATERIAL

See [supplementary material](#) for additional details of calculating resistance, mobility, and diffusion coefficients; implementing constraint dynamics and mean squared displacement analysis for bulk rod diffusion; and empirical fits to position dependent rod diffusion coefficients.

ACKNOWLEDGMENTS

We acknowledge the financial support by the National Science Foundation (No. CBET-1234981).

- G. Li and J. X. Tang, "Diffusion of actin filaments within a thin layer between two walls," *Phys. Rev. E* **69**(6), 061921 (2004).
- M.-H. Lu, L. Feng, and Y.-F. Chen, "Phononic crystals and acoustic metamaterials," *Mater. Today* **12**(12), 34–42 (2009).
- M. J. A. Hore and R. J. Composto, "Nanorod self-assembly for tuning optical absorption," *ACS Nano* **4**(11), 6941–6949 (2010).
- M. Rotunno, T. Bellini, Y. Lansac, and M. A. Glaser, "Phase behavior of polarizable spherocylinders in external fields," *J. Chem. Phys.* **121**(11), 5541–5549 (2004).
- A. Donev, I. Cisse, D. Sachs, E. A. Variano, F. H. Stillinger, R. Connelly, S. Torquato, and P. M. Chaikin, "Improving the density of jammed disordered packings using ellipsoids," *Science* **303**(5660), 990–993 (2004).
- M. J. Solomon and P. T. Spicer, "Microstructural regimes of colloidal rod suspensions, gels, and glasses," *Soft Matter* **6**(7), 1391–1400 (2010).
- K. Chaudhary, J. J. Juarez, Q. Chen, S. Granick, and J. A. Lewis, "Reconfigurable assemblies of Janus rods in AC electric fields," *Soft Matter* **10**(9), 1320–1324 (2014).
- H. Brenner, "The slow motion of a sphere through a viscous fluid towards a plane surface," *Chem. Eng. Sci.* **16**(3-4), 242–251 (1961).
- S. G. Anekal and M. A. Bevan, "Self diffusion in sub-monolayer colloidal fluids near a wall," *J. Chem. Phys.* **125**(3), 034906 (2006).

- ¹⁰S. G. Anekal and M. A. Bevan, "Interpretation of conservative forces from Stokesian dynamic simulations of interfacial and confined colloids," *J. Chem. Phys.* **122**, 034903 (2005).
- ¹¹D. J. Beltran-Villegas, R. M. Sehgal, D. Maroudas, D. M. Ford, and M. A. Bevan, "Fokker-Planck analysis of separation dependent potentials and diffusion coefficients in simulated microscopy experiments," *J. Chem. Phys.* **132**(4), 044707 (2010).
- ¹²E. S. Pagac, R. D. Tilton, and D. C. Prieve, "Hindered mobility of a rigid sphere near a wall," *Chem. Eng. Commun.* **148-150**, 105 (1996).
- ¹³M. A. Bevan and D. C. Prieve, "Hindered diffusion of colloidal particles very near to a wall: Revisited," *J. Chem. Phys.* **113**(3), 1228-1236 (2000).
- ¹⁴R. J. Oetama and J. Y. Walz, "Simultaneous investigation of sedimentation and diffusion of a single colloidal particle near an interface," *J. Chem. Phys.* **124**(16), 164713 (2006).
- ¹⁵D. J. Beltran-Villegas, T. D. Edwards, and M. A. Bevan, "Self-consistent colloidal energy and diffusivity landscapes in macromolecular solutions," *Langmuir* **29**(40), 12337-12341 (2013).
- ¹⁶S. Broersma, "Viscous force and torque constants for a cylinder," *J. Chem. Phys.* **74**(12), 6989-6990 (1981).
- ¹⁷G. K. Batchelor, "Slender-body theory for particles of arbitrary cross-section in Stokes flow," *J. Fluid Mech.* **44**(03), 419-440 (1970).
- ¹⁸M. M. Tirado, C. L. p. Martínez, and J. G. a. de la Torre, "Comparison of theories for the translational and rotational diffusion coefficients of rod-like macromolecules. Application to short DNA fragments," *J. Chem. Phys.* **81**(4), 2047 (1984).
- ¹⁹S. R. Aragon and D. Flamik, "High precision transport properties of cylinders by the boundary element method," *Macromolecules* **42**(16), 6290-6299 (2009).
- ²⁰M. L. Mansfield and J. F. Douglas, "Transport properties of rodlike particles," *Macromolecules* **41**(14), 5422-5432 (2008).
- ²¹Y. Han, A. M. Alsayed, M. Nobili, J. Zhang, T. C. Lubensky, and A. G. Yodh, "Brownian motion of an ellipsoid," *Science* **314**(5799), 626-630 (2006).
- ²²D. Jeffrey and Y. Onishi, "The slow motion of a cylinder next to a plane wall," *Q. J. Mech. Appl. Math.* **34**(2), 129-137 (1981).
- ²³N. J. De Mestre and W. B. Russel, "Low-Reynolds-number translation of a slender cylinder near a plane wall," *J. Eng. Math.* **9**(2), 81-91 (1975).
- ²⁴J. T. Padding and W. J. Briels, "Translational and rotational friction on a colloidal rod near a wall," *J. Chem. Phys.* **132**(5), 054511-054518 (2010).
- ²⁵M. Lisicki, B. Cichocki, and E. Wajnryb, "Near-wall diffusion tensor of an axisymmetric colloidal particle," *J. Chem. Phys.* **145**(3), 034904 (2016).
- ²⁶M. De Corato, F. Greco, G. D'Avino, and P. L. Maffettone, "Hydrodynamics and Brownian motions of a spheroid near a rigid wall," *J. Chem. Phys.* **142**(19), 194901 (2015).
- ²⁷J. F. Brady and G. Bossis, "Stokesian dynamics," *Annu. Rev. Fluid Mech.* **20**(1), 111-157 (1988).
- ²⁸L. Durlofsky, J. F. Brady, and G. Bossis, "Dynamic simulation of hydrodynamically interacting particles," *J. Fluid Mech.* **180**, 21-49 (1987).
- ²⁹J. W. Swan and J. F. Brady, "Simulation of hydrodynamically interacting particles near a no-slip boundary," *Phys. Fluids* **19**(11), 113306 (2007).
- ³⁰E. J. Hinch, "Brownian motion with stiff bonds and rigid constraints," *J. Fluid Mech.* **271**, 219-234 (1994).
- ³¹A. Montesi, D. C. Morse, and M. Pasquali, "Brownian dynamics algorithm for bead-rod semiflexible chain with anisotropic friction," *J. Chem. Phys.* **122**(8), 084903 (2005).
- ³²M. Doi and S. F. Edwards, *The Theory of Polymer Dynamics* (Oxford University Press, 1990).
- ³³S. Kim and S. J. Karrila, *Microhydrodynamics: Principles and Selected Applications* (Dover Publications, 2005).
- ³⁴P. P. Lele, J. W. Swan, J. F. Brady, N. J. Wagner, and E. M. Furst, "Colloidal diffusion and hydrodynamic screening near boundaries," *Soft Matter* **7**(15), 6844-6852 (2011).
- ³⁵A. J. Goldman, R. G. Cox, and H. Brenner, "Slow viscous motion of a sphere parallel to a plane wall—I Motion through a quiescent fluid," *Chem. Eng. Sci.* **22**(4), 637-651 (1967).
- ³⁶C. Sendner and R. R. Netz, "Hydrodynamic lift of a moving nano-rod at a wall," *Europhys. Lett.* **79**(5), 58004 (2007).